

Aerodynamic Coefficients of A Cube in Hypersonic Flow for All Attitudes

Flynn Hack ^{*}, Andrew Lock [†], Gerard Armstrong [‡], Ingo Jahn [§], David Buttsworth [¶] and Fabian Zander ^{||}
University of Southern Queensland, Toowoomba, Queensland, 4360

During re-entry, spacecraft components are often modelled by simple geometries such as cubes, prisms and cylinders, and their aerodynamics have been shown to vary with angle of attack. This work investigates the aerodynamics of a cube in Mach 6 flow for all flight attitudes, as an example of a generic space debris geometry. Forces and moments acting on the cube are calculated using computational fluid dynamics at 16 orientations, which are chosen to exploit symmetry. The data is then extended to 218 independent orientations, covering all possible incident flow angles. Correlations from spherical harmonic basis functions, selected using sparse regression, are then developed for the force and moment coefficients. Regression errors are small relative to previous studies, demonstrating spherical harmonics model the coefficients efficiently. We calculate maximum regression errors of up to 1% and 12% of the maximum force and moment coefficient respectively, compared to 15% and 27% of the maximum force and moment coefficient presented in prior work. The correlations compared well to results from Mach 6 free flight experiments conducted in the TUSQ wind tunnel. The correlations also compared well to published results from Mach 7 free flight experiments conducted in the H2K wind tunnel.

Nomenclature

x^B, y^B, z^B	=	body x, y, z coordinates, m
x^L, y^L, z^L	=	local x, y, z coordinates, m
C_F	=	aerodynamic force coefficient vector
C_M	=	aerodynamic moment coefficient vector
a_c	=	cube side length, m
α'	=	total incidence angle, rad

^{*}PhD Candidate, Institute for Advanced Engineering and Space Sciences, Springfield; flynn.hack@unisq.edu.au

[†]Research Fellow, Institute for Advanced Engineering and Space Sciences, Springfield

[‡]PhD Candidate, Institute for Advanced Engineering and Space Sciences, Toowoomba

[§]Professor, School of Engineering, Springfield, AIAA member

[¶]Professor, School of Engineering, Toowoomba, Senior AIAA member

^{||}Associate Professor, School of Engineering, Toowoomba, AIAA Member; fabian.zander@unisq.edu.au

ϕ'	=	aerodynamic roll angle, rad
r, s	=	unwrapped cube surface coordinates
M	=	Mach number
q_∞	=	dynamic pressure of freestream flow, Pa
Y_l^m	=	spherical harmonic of degree l , order m
$y_{i,j}$	=	spherical harmonic basis function j evaluated at α'_i, ϕ'_i
v_B	=	cube velocity relative to the air, expressed in body coordinates, m/s
λ	=	LASSO regularisation constant
Superscripts		
B	=	body coordinates
L	=	local coordinates

I. Introduction

During uncontrolled re-entry, spacecraft often break apart while travelling at hypersonic speeds. Surviving components are complex geometries which are commonly represented by generic, simple bluff body shapes including cubes, prisms and cylinders. These components create debris fields which can span up to 100s of kilometres [1]. The location of these debris fields is often predicted through 3 degree of freedom (DoF) ballistic trajectory models [2–4], however, these models generally do not consider the object’s flight attitude. Small changes in flight attitude can have a large impact on the aerodynamic lift and drag during re-entry conditions [5, 6]. Therefore, an accurate understanding of the body forces and moments acting on these objects over a range of flight attitudes is important for improving re-entry trajectory predictions.

Seltner et al. [5] measured the aerodynamic forces for a cube in Mach 7 flow, investigating the effect of angle of attack on lift, drag and pitching moments. They measured a pitch axis static stability range of approximately $\pm 27^\circ$, and found a strong dependence between aerodynamics and angle of attack. Lift forces of up to 17% of the maximum drag were observed. Similar measurements have also been made in [6] for cylindrical geometries in Mach 7 flow. Cylinders with a length to diameter ratio of 2 were found to have lift forces of up to 24% of the maximum drag, and maximum lift was measured at pitch angle of 63° . Statically stable trim points with non-zero lift forces were also measured at 21° and 159° . Identifying stable trim points is important for re-entry predictions as ballistic re-entry models fail to capture the effects of lift during flight.

Further key outputs from [5, 6] are correlations for the lift coefficients, drag coefficients, and pitching moment coefficients as a function of angle of attack. Correlations are developed from a linear combination of trigonometric basis functions, which enables efficient aerodynamic predictions as a function of flight attitude, thereby reducing the

resources required for application to re-entry trajectory models. Although correlations in [5, 6] improve upon ballistic trajectory models, only rotation about the object pitching axis is modelled. Correlations for the cylinder can be extended to all flight attitudes (due to the axisymmetric geometry), however, additional data is required to model the forces and moments acting on a cube for all flight attitudes.

Force and moment correlations are commonly developed for hypersonic vehicles, however, longitudinal and lateral aerodynamics are often treated independently due to small angle of attack and sideslip angle operating ranges. This assumption cannot be made for tumbling space debris. Grauer and Morelli [7] approach this task by generating a set of nonlinear, multivariate orthogonal basis functions used in conjunction with linear regression. The candidate regressor variables are orthogonalised and ordered by importance to the data fit, allowing for subset selection of terms for the correlations. Proper orthogonal decomposition [8], singular value decomposition [9, 10] and Chebyshev polynomial [11] approaches have also been used to generate basis functions, however, these approaches result in correlations with significantly more terms [7].

Our work is concerned with angle of attack and sideslip angle, which can be reformulated as spherical coordinates (polar flow angles). Regression is usually performed with polynomial basis functions of these angles [12], however these approaches do not enforce periodicity in the solution. Periodicity is essential for tumbling space debris to ensure there are no discontinuities in the aerodynamic surfaces. Spherical harmonics extend the trigonometric basis functions in [5, 6] to a spherical surface, and provide a set of orthogonal basis functions which enforce periodicity. They have been used for regression in a range of fields, including chemistry [13], molecular modelling [14], and geometry parameterisation [15]. Nortje et al. [15] successfully used spherical harmonics with linear, regularised regression for subset selection, demonstrating applicability to this work.

The goal of this work is to investigate the aerodynamic forces and moments acting on a cube in hypersonic flow, for all flight attitudes. We model a cube in Mach 6 flow to allow for comparison to recent free-flight experiments conducted in The University of Southern Queensland's hypersonic wind tunnel, TUSQ [16, 17] and free-flight experiments conducted in the German Aerospace Centre's (DLR) Hypersonic Wind Tunnel, H2K [5]. First, we use computational fluid dynamics (CFD) to calculate the aerodynamic forces and moments acting on the cube. We then use sparse regression with spherical harmonic basis functions on the numerical data to generate correlations for the force and moment coefficients. Although we choose to investigate a cube in Mach 6 flow, the approach presented in this paper can easily be applied to additional fundamental spacecraft component representative geometries.

The manuscript is structured as follows: In Sec. II of this paper, we describe the numerical approach used to calculate the aerodynamic forces and moments. In Sec. III, we present the regression approach used to develop correlations for the data. The aerodynamic force and moment correlations are presented and discussed in Sec. IV, along with a demonstration of the accuracy compared to free-flight experimental data. Finally, conclusions are drawn and presented in Sec. V.

II. Numerical Approach

A. Quasi-Steady Transient Fluid Solver

Numerical calculations were conducted using the transient, compressible flow CFD solver, Eilmer [18]. The flow is modelled by the compressible Navier-Stokes equation

$$\frac{\partial}{\partial t} \int_V \mathbf{U} dV = - \oint_S (\mathbf{F}_c - \mathbf{F}_v) \cdot \hat{\mathbf{n}} dA + \int_V \mathbf{Q} dV \quad (1)$$

and the air is assumed to be a single species ideal gas. Here, \mathbf{U} is the vector of conserved quantities (mass, momentum and energy), \mathbf{F}_c is the convective flux vector, \mathbf{F}_v is the viscous flux vector and \mathbf{Q} is the source term vector. Following the approach taken in [19, 20], we model viscous effects under the assumption of laminar flow. The Navier-Stokes equations were discretised using a cell centred finite volume approach, and the convective fluxes were calculated using an adaptive flux calculator which selects the AUSMDV scheme [21] away from shocks and the more dissipative Hänel scheme [22] near shocks. Gas dynamics were marched in time using an Euler based predictor-corrector method, in which a global time-step was determined by the Courant-Friedrichs-Lewy (CFL) criterion.

Inflow conditions were taken as the Mach 6 flow condition presented in Sec. II.C, assuming uniform flow acting in the streamwise direction. The flow was also assumed to be steady for each simulation and the cube orientation held fixed. This approach is applicable for trajectories with quasi-steady flow, and is sensible for re-entry conditions due to low spin rates expected. Tumble rates of approximately 4 rpm have been observed for orbital debris in low Earth orbit (LEO), published in the database of photometric periods of artificial satellites [23]. Results from [16] demonstrate the validity of the quasi-steady flow assumption for a 30 mm side-length cube rotating at approximately 600 rpm in Mach 6 flow, which is a much higher spin rate than expected during atmospheric re-entry.

Eilmer's native geometry package was used to discretise the flow domain into a structured mesh with hexahedral elements. An illustration of the mesh is provided in Figure 1. The mesh was constructed by mapping cube surface points to a spherical domain boundary with the elliptical grid mapping technique outlined in [24]. For this work a mesh with radius three times the cube side length was chosen. The effect of this decision is investigated in Sec.II.D. Each cube face was swept to the corresponding spherical face, resulting in 6 identical blocks. This approach ensured flow features were resolved for cell densities independent of the cube orientation, without the need to re-mesh. Desired orientations were achieved by rotating the mesh about the cube centre prior to simulation.

Inflow and outflow at the spherical boundary is modelled by the ghost-cell method. Inflow or outflow is determined by the direction of velocity in the boundary cell (negative flux at the boundary face corresponds to flow entering the domain, and positive flux corresponds to flow leaving the domain). Outflow is modelled by extrapolating the fluid properties of the boundary cells to the ghost cells, which is valid for supersonic flow. The cube walls are assumed to have a constant temperature of 300K, which is reasonable for comparison to impulse facility based experiments over

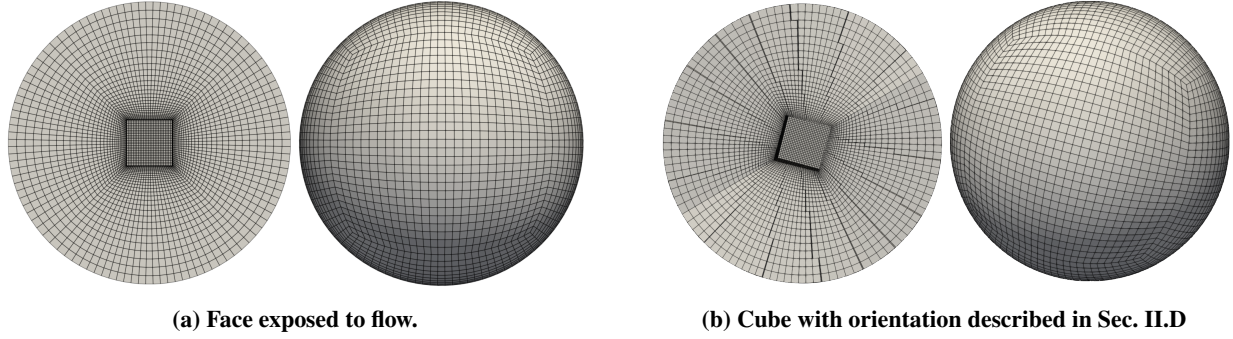


Fig. 1 The computational domain. Cell density is reduced for clarity.

millisecond time-scales.

B. Aerodynamic Force and Moment Coefficients

For this work we use two coordinate systems: local and body-fixed coordinates. Figure 2a depicts the relationship between these coordinates, where s_{BL} is the displacement of the cube centre with respect to the local inertial frame. The cube velocity relative to the incoming flow is expressed in body coordinates, and denoted by $v_B = (u, v, w)^T$. To model aerodynamic forces and moments, we adopt standard polar incident flow angles illustrated in Fig. 2b. Here, the flow angles are defined by the total incidence angle α' and the aerodynamic roll angle ϕ' , where

$$\alpha' = \arccos \left(u / \sqrt{u^2 + v^2 + w^2} \right) \quad (2)$$

$$\phi' = \arctan (v/w) \quad (3)$$

and $\alpha' \in [0, \pi]$, $\phi' \in (-\pi, \pi]$. These angles are similar to a spherical coordinate system for which the polar angle is defined from the x^B axis and azimuth angle is clockwise from the z^B axis. The angles are generally applied to missile applications where the body has rotational symmetry and large angles of attack are expected. This choice of incident flow angles is suitable to exploit the cube's symmetry and model incident flows for all orientations. The polar incident flow angles can also be converted to the standard Cartesian incidence angles by $\alpha = \arctan (\cos \phi' \tan \alpha')$ and $\beta = \arcsin (\sin \phi' \sin \alpha')$, where α is the angle of attack and β is the side-slip angle. Making use of non-dimensional relationships, the aerodynamic forces \mathbf{F} and moments \mathbf{M} (about the cube centre of gravity) were modelled as force,

moment coefficients C_F , C_M

$$[\mathbf{F}]^B = q_\infty a_c^2 \begin{bmatrix} C_{F_x}(M, \alpha', \phi') \\ C_{F_y}(M, \alpha', \phi') \\ C_{F_z}(M, \alpha', \phi') \end{bmatrix}^B \quad (4)$$

$$[\mathbf{M}]^B = q_\infty a_c^3 \begin{bmatrix} C_{M_x}(M, \alpha', \phi') \\ C_{M_y}(M, \alpha', \phi') \\ C_{M_z}(M, \alpha', \phi') \end{bmatrix}^B \quad (5)$$

where $q_\infty = \frac{1}{2}\rho_\infty \|\mathbf{v}_B\|^2$ is the free-stream dynamic pressure, a_c is the cube side length and the coefficients are defined in body coordinates. For this work we develop correlations for the six coefficients, valid for all α' and ϕ' and a single Mach number M .

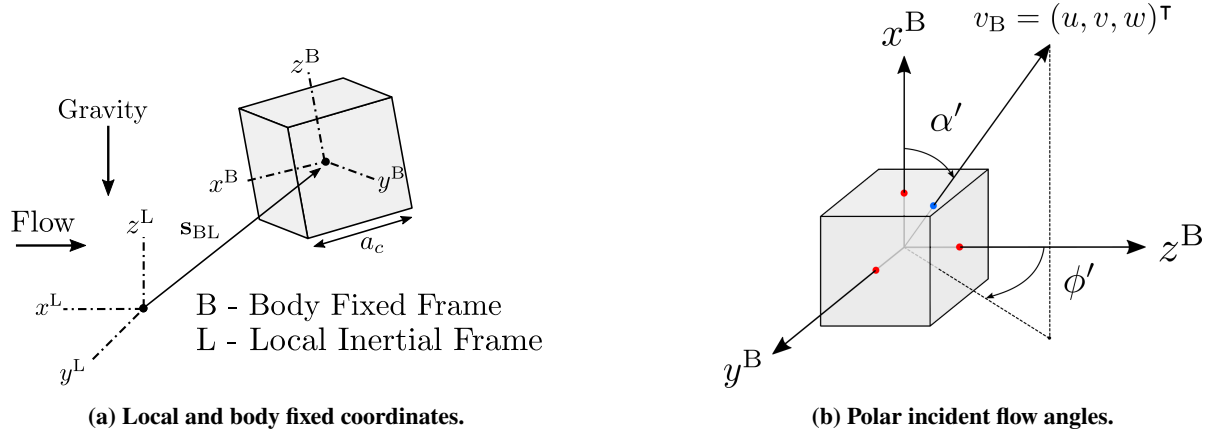


Fig. 2 Coordinate systems used in this work.

C. Simulation Matrix and Free-stream Flow Condition

The simulations presented in this work were conducted using the nominal Mach 6 test condition for the University of Southern Queensland’s hypersonic wind tunnel, TUSQ [25], illustrated in Table 1. This condition is well characterised [26–28] and in close agreement with the conditions achieved in free-flight experiments conducted in parallel to this work [16], for which experimental data is available. For a fixed Reynolds number and Mach number, the condition is equivalent to a 30 mm side-length cube flying at 23.3km altitude, or a 5U CubeSat at 41.3km altitude, which is reasonable for re-entry applications. This scaling is calculated using properties from the 1993 International Civil Aviation Organisation standard atmosphere model [29]. Aerodynamic coefficients are calculated for incident flow angles selected by considering the location where \mathbf{v}_B intersects the cube surface, denoted by r , s (see Fig. 2b). Figure 3 demonstrates this concept, whereby the cube surface is “unwrapped” and described in two-dimensional space. This

Table 1 Nominal free-stream flow conditions.

Parameter	Nominal Value
p_0 [kPa]	1000
T_0 [K]	575
p_∞ [Pa]	670
T_∞ [K]	71
v_∞ [m s ⁻¹]	1006
ρ_∞ [kg m ⁻³]	0.0327
Re_{unit} [m ⁻¹]	$6.50 \cdot 10^6$

approach allows for greater consideration of the geometry of the object when sampling the aerodynamics, and enables easy exploitation of the cube shape symmetry.

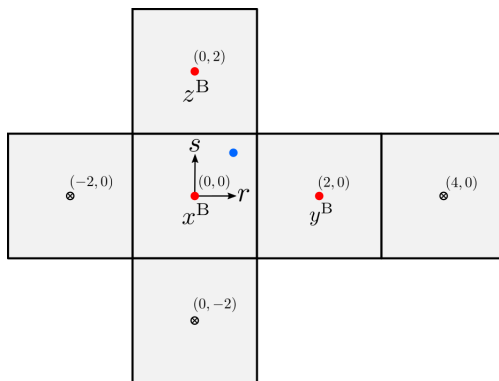


Fig. 3 Unwrapped surface coordinates. The blue dot represents the r, s coordinate associated with the incident flow vector in Fig. 2b.

The frontal cube face is defined by surface coordinates $r, s \in [-1, 1]$. We present results from 16 simulations with cube orientations corresponding to a 4×4 mesh-grid of evenly spaced points in $r, s \in [0, 1]$. These orientations cover a quarter cube face and are chosen to align with the cube symmetry planes, enabling replication of the results to all possible cube orientations. Results from 8 additional simulations not used in regression are also presented in Sec. IV.D.2 for comparison to the correlations.

D. Mesh Independence of Results

A mesh refinement study was completed to ensure sufficient resolution of flow features relevant to the cube aerodynamics. The study was completed using the methodology described in [30] and [31], with three grid refinement levels, coarse, medium and fine. Grid refinement was achieved by increasing the number of cells along each axis of the parameterised mesh. While care was taken to minimise the y^+ parameter for cells adjacent to the cube wall, a strict limit of $y^+ < 1$ for all cells was not enforced. As viscous forces only accounted for a small portion of the total force acting on the cube ($< 1\%$), this was deemed appropriate.

The mesh refinement study considers a cube with incident flow defined by $\alpha' = 97.1^\circ$, $\phi' = -83.1^\circ$, corresponding to an arbitrary cube orientation measured in [16]. Although this study does not guarantee mesh independence for all orientations, a much wider range of experimental data was used to validate the computational approach in later parts of this work. Starting with the coarsest mesh, constant scaling factors of 2 and 3 were applied along each cell direction for the medium and fine mesh refinement levels respectively. A larger mesh with radius four times the cube side length and a fine refinement level was also generated to investigate the effect of domain size.

Results for the refinement study are outlined in Table 2. Force coefficients are asymptotically convergent with increasing cell density, whereas oscillatory convergence is observed for the body moment coefficients as cell density increases. The larger domain results in a maximum force coefficient difference of 0.001 and a maximum moment coefficient difference of 0.0003 relative to the fine mesh. The domain size three times the cube side length was considered appropriate for this work. The flow-field around the cube simulated using the fine mesh is shown in Fig. 4. The highest pressure region is on the frontal face after the flow stagnates behind the bow shock. Expansion fans caused by the flow passing the sharp cube edges are visible, creating low pressures on the faces in the wake regions and density gradients in the flow-field. These results provide confidence in the numerical model, and the fine grid refinement level was chosen for all simulations completed herein.

Table 2 Effect of mesh density on force and moment coefficients.

Mesh	No. Cells	C_{Fx^L}	C_{Fy^L}	C_{Fz^L}	C_{Mx^B}	C_{My^B}	C_{Mz^B}
Coarse	1.18×10^5	-1.671	-0.155	-0.095	-0.0131	0.0000	-0.0136
Medium	9.45×10^5	-1.667	-0.150	-0.092	-0.0144	-0.0001	-0.0149
Fine	3.19×10^6	-1.667	-0.147	-0.091	-0.0144	-0.0001	-0.0147
Fine (large domain)	4.25×10^6	-1.666	-0.147	-0.090	-0.0142	0.0000	-0.0144

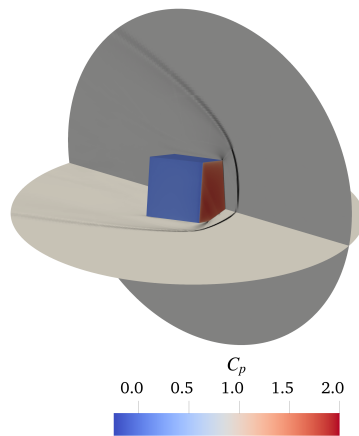


Fig. 4 Cube flow-field on the fine grid. Incoming flow is parallel to the vertical slice.

III. Regression of Aerodynamic Coefficients

A. Spherical Harmonic Basis Functions

We use real-valued basis functions defined by spherical harmonics to model aerodynamic force and moment coefficients. Spherical harmonic basis functions have worked well with regularised regression [15], and were chosen to extend the approach in [5] to cube orientations defined by multiple angles. As our polar incident flow angles (α', ϕ') form a spherical coordinate system (where the polar angle is defined relative to the x^B axis), spherical harmonic basis functions were expected to capture the shape of aerodynamic curves effectively. These basis functions also enforce repetition about angle bounds, ensuring no discontinuities are present for a tumbling cube. Spherical harmonics of degree l and order m are described by

$$Y_l^m(\alpha', \phi') = \sqrt{\frac{2l+1}{4\pi} \frac{(l-m)!}{(l+m)!}} P_l^m(\cos \alpha') e^{im\phi'} \quad (6)$$

where l is a positive integer, m is an integer ($|m| \leq l$) and P_l^m is an associated Legendre Polynomial defined by Eq. (7). Guidance on the evaluation and properties of the associated Legendre Polynomials is provided in [32].

$$P_l^m(x) = \frac{(-1)^m}{2^l l!} (1-x^2)^{m/2} \frac{d^{l+m}}{dx^{l+m}} (x^2-1)^l \quad (7)$$

To construct our matrix of regressors, we choose basis functions with a maximum degree l_{\max} for our spherical harmonics, and consider all possible orders m ($|m| \leq l$) for $l \leq l_{\max}$. This approach provides k basis functions, where $k = (l_{\max} + 1)^2$, and is similar to [15]. We define the j^{th} basis function using a unique indexing for each pair (l, m) defined by $j = l^2 + l + m + 1$, evaluated at α'_i, ϕ'_i by

$$y_{i,j} = \begin{cases} \sqrt{2} (-1)^m \Im [Y_l^{|m|}(\alpha'_i, \phi'_i)] & m < 0 \\ Y_l^0(\alpha'_i, \phi'_i) & m = 0 \\ \sqrt{2} (-1)^m \Re [Y_l^m(\alpha'_i, \phi'_i)] & m > 0 \end{cases} \quad (8)$$

where scaling of the basis functions retains orthogonality. An illustration of the basis functions for $l_{\max} = 2$ is given in Fig. 5. Our matrix of regressors \mathbf{X} is

$$\mathbf{X} = \begin{pmatrix} y_{1,1} & y_{1,2} & \cdots & y_{1,k} \\ y_{2,1} & y_{2,2} & \cdots & y_{2,k} \\ \vdots & \vdots & \ddots & \vdots \\ y_{n,1} & y_{n,2} & \cdots & y_{n,k} \end{pmatrix} \quad (9)$$

where n is the number of sampled data points. For this work, spherical harmonics of $l_{\max} = 10$ were used for regression, yielding 121 candidate basis functions. Harmonics with $l_{\max} = 10$ were found to work well based on an iterative approach. Negligible improvements in regression were observed for basis functions of higher degree.

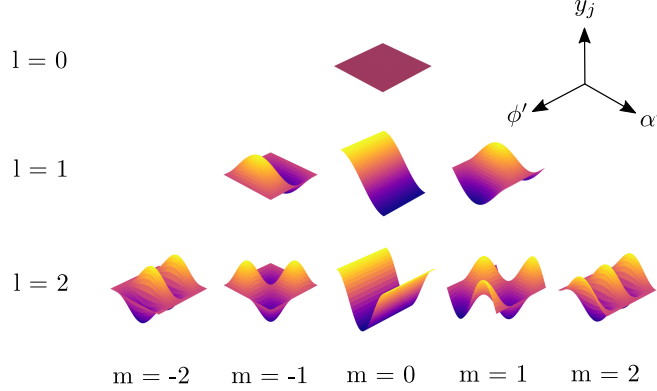


Fig. 5 Spherical harmonic basis functions for $l_{\max} = 2$.

B. Regression Approach

Sparse regression implementing the LASSO algorithm [33] was used to identify a subset of terms which provide the highest correlation to the force and moment coefficient data. LASSO regularises least squares regression by the L1 norm of regression coefficients and was chosen primarily to promote sparsity in the final model. The regression coefficients are calculated by

$$\boldsymbol{\beta}^* = \underset{\boldsymbol{\beta}}{\operatorname{argmin}} \{ \|\boldsymbol{f} - \boldsymbol{X}\boldsymbol{\beta}\|_2^2 + \lambda \|\boldsymbol{\beta}\|_1 \} \quad (10)$$

where \boldsymbol{f} is a vector of force or moment coefficients, $\boldsymbol{\beta}$ is a vector of regression coefficients, λ is the regularisation constant and \boldsymbol{X} is a matrix of basis function evaluations. The regularisation constant was selected using the following approach for each coefficient C_{Fi} , C_{Mi} , where $i = x^B, y^B$ or z^B . LASSO regression was performed for a range of λ , and the number of non-zero regression terms were compared to the root mean squared error (RMSE). A final λ was then chosen to balance RMSE magnitude and regression terms. After using LASSO for subset selection, the basis functions with non-zero regression coefficients were regressed against the data using (unregularised) least squares regression to determine their best fit coefficients. This regression approach is effective for engineering correlation term selection [34], and is demonstrated for $C_{F_{x^B}}$ in Figure 6. Here the RMSE is expressed as a raw value.

As expected, the number of non-zero regression coefficients reduces with increasing λ , while the RMSE increases significantly after λ reaches a threshold. Figure 6 demonstrates a suitable selection of λ can be made by balancing the RMSE and the complexity of the model (number of basis functions to evaluate). In practice, λ was selected conservatively as the benefit of reducing the model complexity is smaller than the cost of introducing unnecessary regression error. Specifically, $\lambda = 10^{-4}$ and $\lambda = 10^{-5}$ were chosen for all C_{Fi} and C_{Mi} respectively.

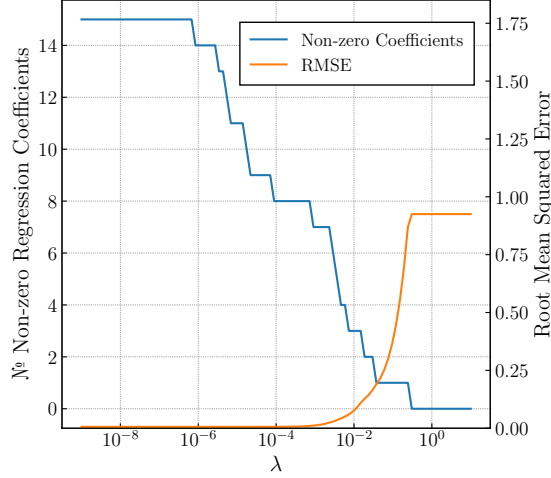


Fig. 6 Regularisation coefficient λ vs the number of non-zero regression coefficients for $C_{F_{xB}}$.

IV. Results and Discussion

A. CFD Calculations

Force and moment coefficient data was collected by performing the 16 simulations described in Sec. II.C. The simulations were conducted using the University of Southern Queensland’s Fawkes high performance computing facility. Each simulation used 81 AMD EPYC7702 CPU cores and 200GB of allocated memory, with an average wall clock time of 14.1hrs. A qualitative illustration of the results is provided in Fig. 7, where magnitude of density gradient is plotted on the vertical flow slices, coefficient of pressure is plotted on the cube surfaces and flow is going into the page. Symmetry is clearly present in the flow-fields, and cube orientation has a large effect on surface pressure. Flow-fields for $s = 0$ appear identical to flow-fields for $r = 0$ rotated by 90° about the x^L axis. Symmetry in the flow-fields mirrors the cube shape symmetry and provides confidence in the reduced simulation matrix chosen for this work.

Prior to regression, aerodynamic coefficients were extended to symmetrically similar orientations by flipping and rotating the data about symmetry planes. One example of this is a rotation of 90° , which enables the extension $C_{F_{xB}}(\alpha' = 0, \phi' = 0) = C_{F_{zB}}(\alpha' = \pi/2, \phi' = 0)$. With appropriate flipping and rotation, we found the entire range of incident flow angles could be replicated from orientations covering an eighth of the cube face defined by the triangle with vertices $(r, s) = (0, 0), (1, 1), (1, 0)$ (see Fig. 7). Nonetheless, our CFD data for the quarter cube face $(r, s \in [0, 1])$ was extended to define the forces and moments over all incident flow angles. This extension is demonstrated in Fig. 8, where 16 simulations were extended to 218 independent flow orientations, significantly reducing the computational cost compared to simulating the entire range of possible orientations.

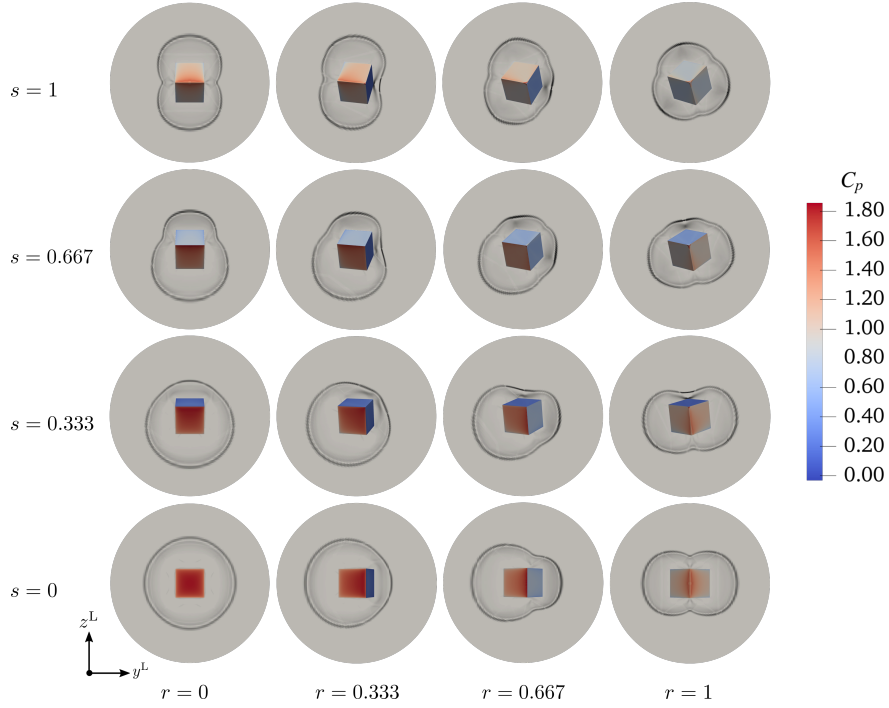


Fig. 7 CFD flow-fields; flow is going into the page and the density gradient is plotted on the vertical flow slice.

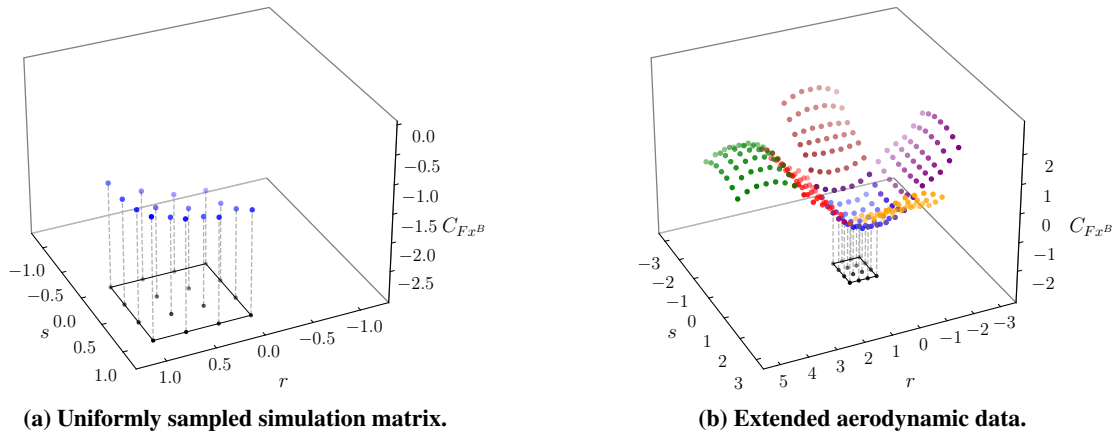


Fig. 8 Data extension for $C_{F_{x^B}}$; colours in (b) change for each cube face.

B. Aerodynamic Coefficient Correlations

Correlations for force and moment coefficients are developed using the methodology described in Sec. III. Figure 9 provides an illustration of the six correlations (surfaces) and the extended CFD results (blue circles). Both aerodynamic forces and moments are periodic, and the correlations appear to be in good agreement with the CFD results. Spherical harmonics with degree $l = 1$ (see Fig. 5) closely resemble the force coefficients, while harmonics with degree $l = 4$ resemble the moment coefficients. The moments oscillate at a higher frequency compared to the forces, and values m and $l - |m|$ relate to the frequency of oscillations in ϕ' and α' respectively. A $\phi' = 90^\circ$ phase shift is present between

forces and moments in the y^B and z^B coordinates (e.g. $C_{F_{y^B}}$ and $C_{F_{z^B}}$). This phase shift is expected as the polar flow angle ϕ' lies in the y^B, z^B plane, and the y^B, z^B axes are 90° apart. These expected trends provide confidence in the application of the symmetry operations used to extend the data.

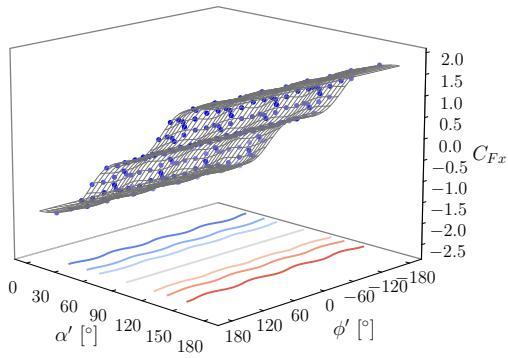
Regression coefficients are presented in Table 3, and an example of their use is provided in a code repository*. For each surface, harmonics with the largest regression coefficient match the expected shape well. These primary harmonics are $(l, m) = (1, 0), (1, -1)$ and $(1, 1)$ for forces in the x^B, y^B and z^B coordinates respectively. Primary harmonics for the moment coefficients are $(l, m) = (4, -4), (4, 1)$ and $(4, -1)$ for moments in the x^B, y^B and z^B coordinates respectively. LASSO regression with spherical harmonic basis functions modelled the data efficiently, selecting 8 and 11 harmonics from 121 basis functions for $C_{F_{x^B}}$ and $C_{M_{x^B}}$ respectively. Coefficients $C_{F_{y^B}}, C_{F_{z^B}}$ were modelled by 15 harmonics, and $C_{M_{y^B}}, C_{M_{z^B}}$ were modelled by 25 harmonics. In similar work, the pitching moment coefficient of a cylinder about a single axis was modelled with 6 Fourier coefficients [6].

Table 3 Regression coefficients for the aerodynamic correlations. $\beta_{(l,m)}$ is the regression coefficient of Eq. (8) defined by degree l and order m .

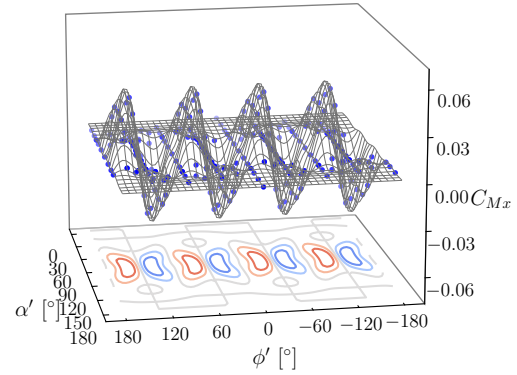
$C_{F_{x^B}}$	$C_{F_{y^B}}$	$C_{F_{z^B}}$	$C_{M_{x^B}}$	$C_{M_{y^B}}$	$C_{M_{z^B}}$
$\beta_{(1,0)} = -3.2608$	$\beta_{(1,-1)} = -3.2609$	$\beta_{(1,1)} = -3.2609$	$\beta_{(3,2)} = -0.0010$	$\beta_{(3,-3)} = -0.0006$	$\beta_{(3,1)} = -0.0008$
$\beta_{(3,0)} = -0.4250$	$\beta_{(3,-3)} = 0.3359$	$\beta_{(3,1)} = 0.2601$	$\beta_{(4,-4)} = -0.0584$	$\beta_{(3,-1)} = 0.0008$	$\beta_{(3,3)} = -0.0006$
$\beta_{(5,0)} = 0.3313$	$\beta_{(3,-1)} = 0.2603$	$\beta_{(3,3)} = -0.3360$	$\beta_{(5,2)} = -0.0012$	$\beta_{(4,1)} = -0.0546$	$\beta_{(4,-3)} = 0.0206$
$\beta_{(5,4)} = 0.0659$	$\beta_{(5,-5)} = 0.2458$	$\beta_{(5,1)} = 0.1987$	$\beta_{(6,-4)} = 0.0090$	$\beta_{(4,3)} = 0.0206$	$\beta_{(4,-1)} = 0.0546$
$\beta_{(7,0)} = -0.0483$	$\beta_{(5,-3)} = 0.1207$	$\beta_{(5,3)} = -0.1208$	$\beta_{(7,2)} = -0.0004$	$\beta_{(5,-5)} = 0.0008$	$\beta_{(5,1)} = 0.0008$
$\beta_{(7,4)} = 0.0301$	$\beta_{(5,-1)} = 0.1981$	$\beta_{(5,5)} = 0.2455$	$\beta_{(8,-8)} = 0.0117$	$\beta_{(5,-3)} = -0.0004$	$\beta_{(5,3)} = -0.0004$
$\beta_{(9,0)} = -0.0347$	$\beta_{(7,-7)} = 0.0224$	$\beta_{(7,1)} = 0.0038$	$\beta_{(8,-4)} = 0.0049$	$\beta_{(5,-1)} = -0.0008$	$\beta_{(5,5)} = -0.0008$
$\beta_{(9,8)} = 0.0121$	$\beta_{(7,-5)} = 0.0468$	$\beta_{(7,3)} = -0.0240$	$\beta_{(9,2)} = 0.0012$	$\beta_{(6,1)} = -0.0039$	$\beta_{(6,-5)} = -0.0053$
	$\beta_{(7,-3)} = 0.0243$	$\beta_{(7,5)} = 0.0466$	$\beta_{(9,6)} = 0.0011$	$\beta_{(6,3)} = -0.0062$	$\beta_{(6,-3)} = -0.0061$
	$\beta_{(7,-1)} = 0.0042$	$\beta_{(7,7)} = -0.0229$	$\beta_{(10,-8)} = -0.0098$	$\beta_{(6,5)} = 0.0053$	$\beta_{(6,-1)} = 0.0039$
	$\beta_{(9,-9)} = -0.0197$	$\beta_{(9,1)} = -0.0069$	$\beta_{(10,-4)} = -0.0030$	$\beta_{(7,-3)} = 0.0002$	$\beta_{(7,3)} = 0.0002$
	$\beta_{(9,-7)} = -0.0183$	$\beta_{(9,3)} = 0.0219$		$\beta_{(8,1)} = 0.0111$	$\beta_{(8,-7)} = -0.0037$
	$\beta_{(9,-5)} = -0.0081$	$\beta_{(9,5)} = -0.0081$		$\beta_{(8,3)} = -0.0031$	$\beta_{(8,-5)} = -0.0038$
	$\beta_{(9,-3)} = -0.0216$	$\beta_{(9,7)} = 0.0182$		$\beta_{(8,5)} = 0.0038$	$\beta_{(8,-3)} = -0.0030$
	$\beta_{(9,-1)} = -0.0072$	$\beta_{(9,9)} = -0.0204$		$\beta_{(8,7)} = -0.0036$	$\beta_{(8,-1)} = -0.0110$
				$\beta_{(9,-9)} = -0.0009$	$\beta_{(9,1)} = -0.0011$
				$\beta_{(9,-7)} = 0.0005$	$\beta_{(9,3)} = 0.0002$
				$\beta_{(9,-5)} = -0.0004$	$\beta_{(9,5)} = 0.0004$
				$\beta_{(9,-3)} = 0.0002$	$\beta_{(9,7)} = 0.0005$
				$\beta_{(9,-1)} = 0.0011$	$\beta_{(9,9)} = 0.0009$
				$\beta_{(10,1)} = 0.0051$	$\beta_{(10,-9)} = 0.0030$
				$\beta_{(10,3)} = 0.0045$	$\beta_{(10,-7)} = 0.0044$
				$\beta_{(10,5)} = -0.0055$	$\beta_{(10,-5)} = 0.0054$
				$\beta_{(10,7)} = 0.0044$	$\beta_{(10,-3)} = 0.0045$
				$\beta_{(10,9)} = -0.0029$	$\beta_{(10,-1)} = -0.0051$

Maximum values $C_{F_i} = 1.70$ and $C_{M_i} = 0.045$ are predicted by the correlations. Maximum force coefficients occur at cube orientations where the face is normal to the flow, while the maximum moment coefficients occur when cube faces are oblique to the flow. These results are in good agreement with the maximum drag coefficient of 1.71 in [5] and 1.66 from Hoerner [35], and the maximum pitching moment coefficient of 0.043 in [5].

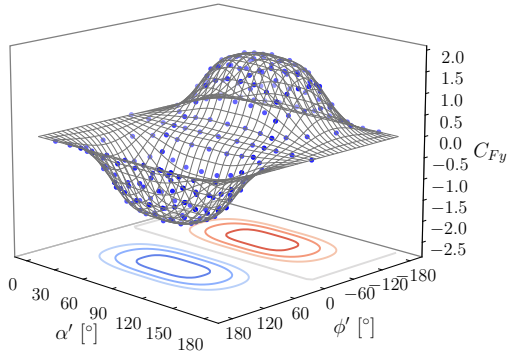
*https://github.com/flynnh-github/Cube_AeroDeck_M6



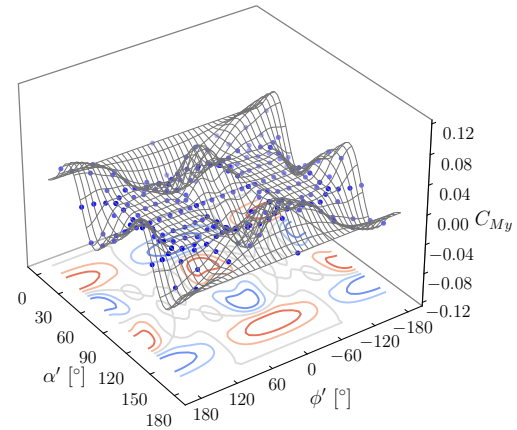
(a) $C_{F_x B}(\alpha', \phi')$



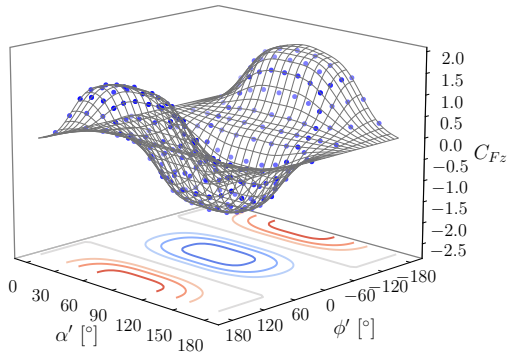
(b) $C_{M_x B}(\alpha', \phi')$



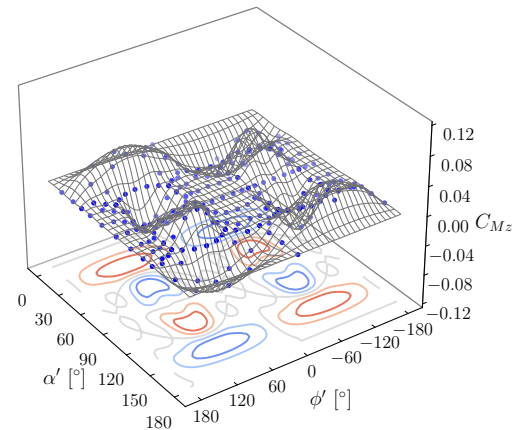
(c) $C_{F_y B}(\alpha', \phi')$



(d) $C_{M_y B}(\alpha', \phi')$



(e) $C_{F_z B}(\alpha', \phi')$



(f) $C_{M_z B}(\alpha', \phi')$

Fig. 9 Force and moment coefficient curves. The surface is sampled from the correlations and the markers correspond to the CFD data.

C. Fitting Error Introduced by Regression

A comparison between the CFD data and regression correlations is presented in Fig. 10. The solid line represents a perfect match between the CFD data and coefficients predicted by the correlations.

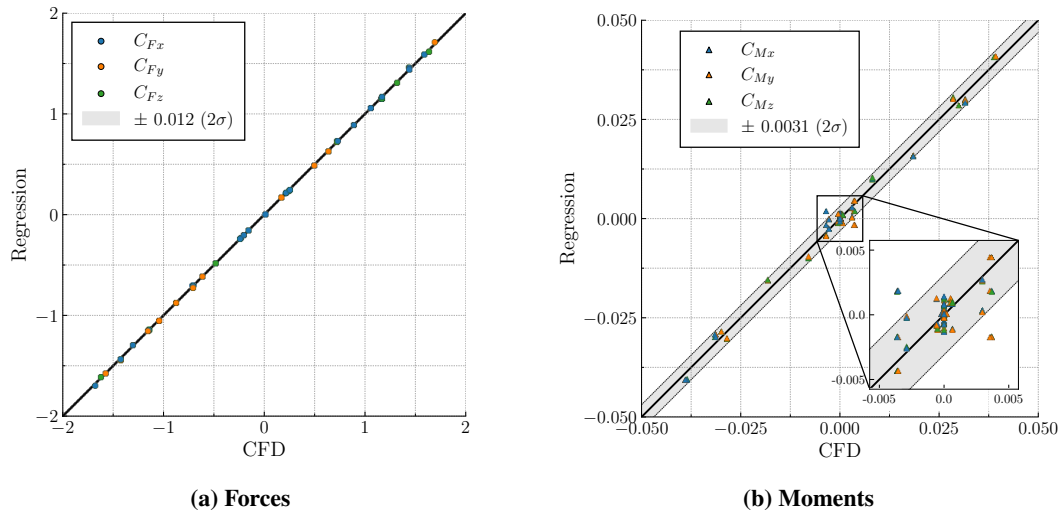


Fig. 10 Comparison of the CFD data and correlations, where σ is the standard deviation of the grouped regression error terms ΔC_{Fi} or ΔC_{Mi} .

Predictions from the force correlations are in good agreement with CFD results, and the maximum regression error is $\Delta C_{Fi} = 0.019$. A confidence interval (CI) spanning $\pm 2\sigma$ of the sample points is $C_{Fi} \pm 0.012$, where σ is the standard deviation of the grouped regression error terms. Moment correlations have larger relative regression error than the forces, and maximum regression errors occur for small moments $-0.01 \leq C_{Mi} \leq 0.01$. A maximum $\Delta C_{Mi} = 0.0054$ is observed, and the CI spanning $\pm 2\sigma$ is $C_{Mi} \pm 0.0031$.

A 3σ range of the regression error distribution is 1% of the maximum C_{Fi} , and 12% of the maximum C_{Mi} . This is a significant improvement compared to 3% of the maximum C_D , 15% of the maximum C_L and 27% of the maximum C_M reported in prior work [5]. However, these improvements are likely exaggerated due to differences in the uncertainty associated with the underlying data (experimental data is presented in [5] and numerical calculations are presented in this work). Nevertheless, the regression error is small, and the correlations presented in this work model the data well. These results demonstrate LASSO regression with spherical harmonic basis functions provides an improvement over former approaches.

D. Comparison of Correlations to Experimental Data

To quantify the accuracy of our correlations, we provide a comparison to two sets of experimental data: (1) Mach 6 TUSQ free-flight experiments over a range of cube orientations; and (2) Mach 7 free-flight experiments of a cube rotating about the pitch axis, presented in [5]. Optical measurements are captured with two high speed cameras for both

datasets. In (1), detected cube features are treated as system observations and a sigma-point Kalman filter is used to estimate the cube state and hence aerodynamic forces and moments. In (2), three dimensional points are reconstructed via stereoscopic triangulation, after which the cube position and attitude are estimated via digital image correlation. Smoothing operations and numerical differentiation are then employed to calculate the cube accelerations, and hence aerodynamic forces and moments. Comparison to these datasets is discussed below.

1. Comparison to TUSQ Free Flight Experiments

Our aerodynamic correlations are compared to results from free-flight experiments presented in [16, 17], conducted in parallel to this work. The experiments consisted of 4 wind-tunnel runs, where a 30 mm side-length cube was released at varied orientations relative to the flow direction. The cube was spun to approximately 600 rpm for the final run, ensuring the aerodynamics were measured for a large sweep of incident flow angles. Figure 11 shows a comparison between the incident flow angles for which experimental data is available (red markers) and the CFD simulation matrix (blue markers). Large discontinuities in the experimental data correspond to a new run. Figure 12 provides an illustration of the experimental data (red markers) compared to our correlations (surfaces). Figure 13 provides a histogram of the differences between correlations and experiments. The experimental data was extended using symmetry, and we compare the magnitudes of each measurement ($\|\mathbf{C}_F\|$ or $\|\mathbf{C}_M\|$) to preserve biases in the distribution of the differences $\Delta\|\mathbf{C}_F\|$, $\Delta\|\mathbf{C}_M\|$.

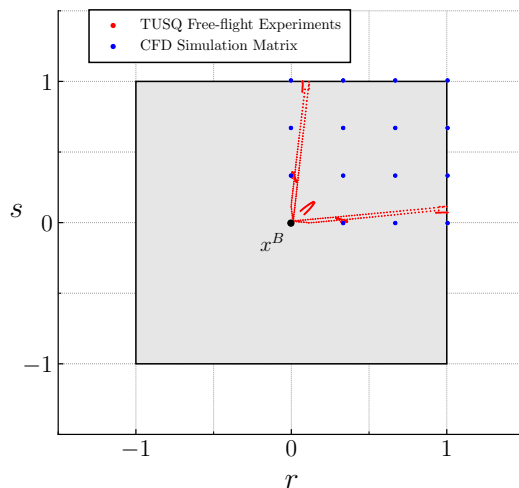
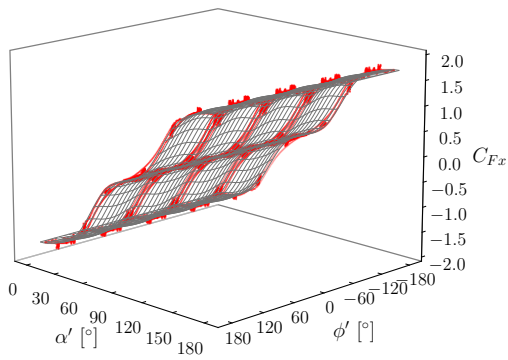
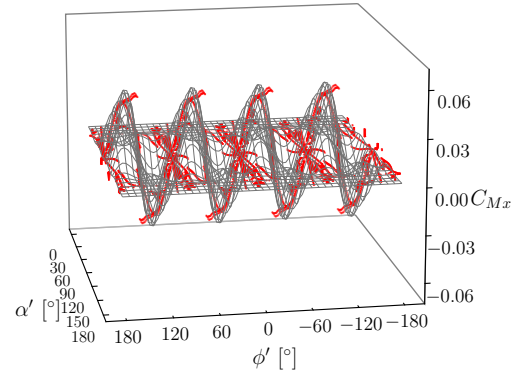


Fig. 11 Incident flow angles for $0 \leq r, s \leq 1.0$. Large discontinuities correspond to a new experiment.

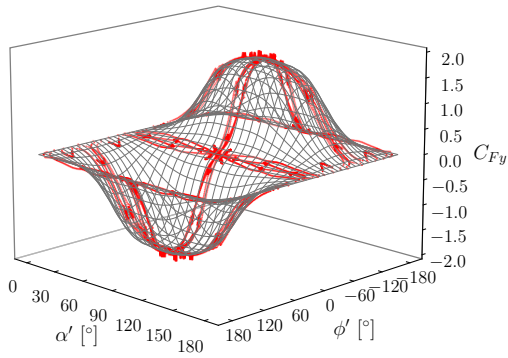
The correlations are in close agreement with experimental data for the majority of flow angles. Maximum differences of $\Delta\|\mathbf{C}_F\| = 0.12$ and $\Delta\|\mathbf{C}_M\| = 0.032$ are observed. The mean of the force coefficient differences is $\overline{\Delta\|\mathbf{C}_F\|} = 0.03$, and the mean of the moment coefficient differences is $\overline{\Delta\|\mathbf{C}_M\|} = 0.002$. Although the maximum $\Delta\|\mathbf{C}_M\| = 0.032$ is significant when compared to the maximum $\|\mathbf{C}_M\| = 0.045$, this value corresponds to outliers in the experimental data.



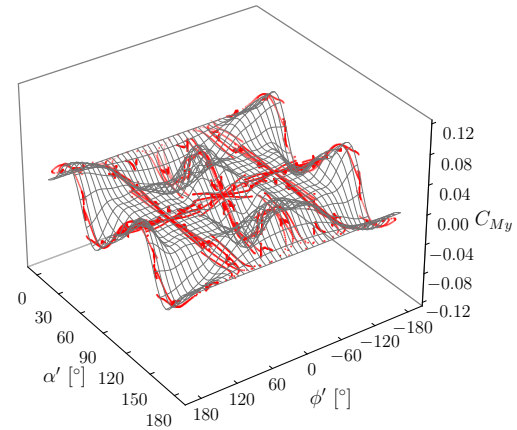
(a) $C_{Fx\text{B}}(\alpha', \phi')$



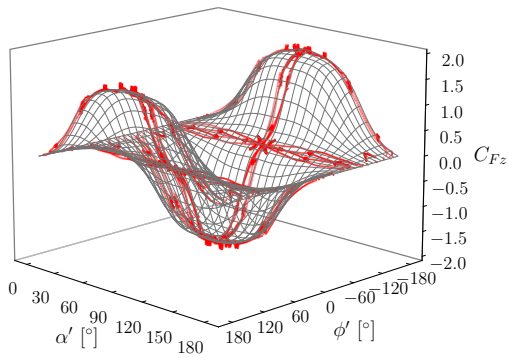
(b) $C_{Mx\text{B}}(\alpha', \phi')$



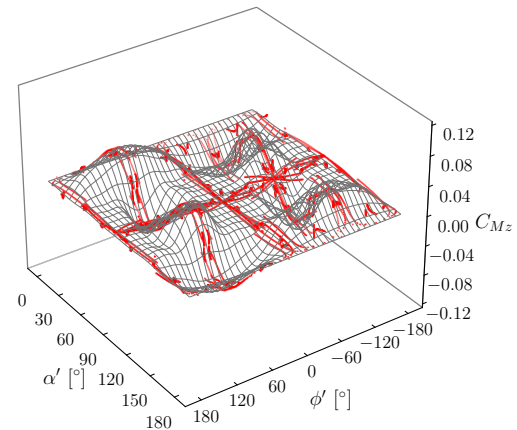
(c) $C_{Fy\text{B}}(\alpha', \phi')$



(d) $C_{My\text{B}}(\alpha', \phi')$



(e) $C_{Fz\text{B}}(\alpha', \phi')$



(f) $C_{Mz\text{B}}(\alpha', \phi')$

Fig. 12 Coefficient correlations compared to TUSQ free-flight experimental results. The surface represents the correlations and the red markers illustrate the experimental data.

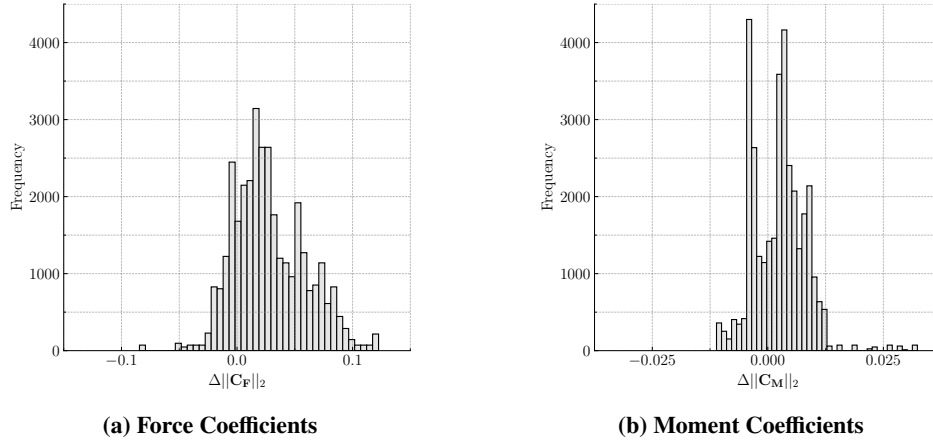


Fig. 13 Histogram comparing the aerodynamic correlations and the experimental data presented in [16].

Outliers repeat over multiple angle sweeps due to the extension of the data, and largely originate from measurements in a 3 ms window of the spinning cube run, as discussed in [16, 17].

The authors of [16, 17] provide discussion on the limitations of the experimental data for comparison to ideal cube simulations. Foremost is the difference in cube geometry, which had chamfered corners during the cube experiments. There is also measurement uncertainty in the optical tracking methodology, estimated to be 0.6% and 4.7% of the maximum force and moment coefficients respectively for low rotation axes, and 3.4% and 26.8% of the maximum force and moment coefficients respectively for high rotation axes [17]. Contributions from generalised sources such as the cube mass and free-stream flow are not discussed in [17]. Additionally, modelling assumptions are made in the numerical approach. The assumption of laminar flow and smooth surfaces may fail to capture turbulent flow effects present in the experiments which may have a material effect on the forces and moments. Finally, although the mesh independence results in Sec. II.D indicate convergence for one orientation, convergence over all orientations is not guaranteed.

When comparing these data-sets, it is also worth noting the experimental data primarily covers regions where $r \approx 0$ or $s \approx 0$. The error distributions are independent of the incident flow angles for the comparison, so the findings are assumed to hold for all incident flow angles until additional experimental data becomes available. Overall, considering the regression error, the impact of assumptions used in the numerical simulations, and the uncertainties in the experimental results, this comparison gives confidence in the quality and value of the correlations.

2. Comparison to Mach 7 H2K Free Flight Experiments

Our aerodynamic correlations are compared to a second experimental dataset generated from free-flight experiments performed in the German Aerospace Centre’s (DLR) Hypersonic Wind Tunnel (H2K) at Mach 7 flow conditions [5]. Cubes are fixed above the core flow by an electromagnet. A pitching moment is generated on contact with the core flow,

spinning the cube. For this comparison, we also provide results from 8 CFD simulations sampled in 5° increments. These additional CFD results were not used in the regression, and are presented to investigate the accuracy of the correlations further. The comparison is provided Fig. 14 and is presented as a function of the Cartesian angle of attack α for simplicity. Orientations of the cube in the x^L, z^L plane are overlaid, as seen looking along the y^L axis.

Both sets of CFD data show strong agreement with the experimental data over all angles. Agreement between Mach 6 and Mach 7 results suggests the aerodynamic coefficients are approaching Mach number independence for our simulations. The maximum force coefficient $|C_{F_{x^L}}| = 1.70$ occurred for the cube face normal to the flow, and is in strong agreement to the value 1.71 in [5] and 1.66 from [35]. Strong agreement is also shown for $C_{F_{z^L}}$, as demonstrated by the maximum difference $\Delta C_{F_{z^L}} = 0.01$ relative to [5]. The maximum $C_{F_{z^L}}$ occurs at $\alpha = \pm 21.7^\circ$, and is in good agreement with the maximum lift location $\alpha = \pm 22.5^\circ$ reported in [5].

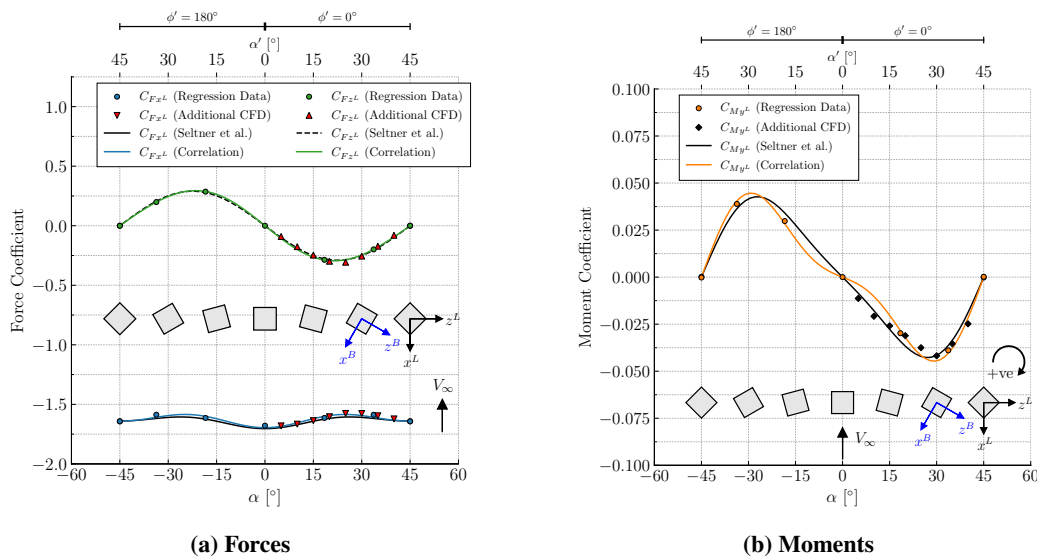


Fig. 14 Force and moment coefficients compared to [5]. The cube orientation relative to the flow is shown by the overlaid cubes (as seen looking parallel to the y^L axis).

Our correlations predict a maximum $|C_{M_{y^L}}| = 0.045$, which is in strong agreement compared to the maximum pitching moment of 0.043, presented in [5]. Maximum $C_{M_{y^L}}$ occurs at $\alpha = \pm 29.5^\circ$ compared to $\alpha = \pm 27^\circ$ in [5]. The maximum difference between our correlations and results in [5] is $\Delta C_{M_{y^L}} = 0.008$, occurring between $-25^\circ \leq \alpha \leq 25^\circ$ (where the angle spacing between the regression data is largest). The CFD results not used in correlation development more closely match the experimental data in these regions, suggesting some improvements to our correlations may be possible. Increasing the number of CFD calculations used to develop the correlations is one such improvement. Furthermore, the additional CFD was sampled uniformly in α , while the simulation matrix was sampled uniformly in r, s coordinates. Some benefits may also be realised by non-uniform grid sampling approaches.

There are also limitations in the experimental data for comparison to ideal cube simulations (see [5] for discussion).

Foremost is measurement uncertainty of the optical tracking algorithm. Uncertainty is present in feature detection and digital image correlation for position and pose identification, increasing for measurements near the edge of the viewing field where poor lighting was present. Smoothing operations before and after numerical differentiation add additional uncertainty in the dataset, however, no estimates for the magnitude are provided in [5]. Cube motion is also assumed planar, however, roll and yaw angles up to approximately 2° were measured during experiments. Generalised sources of uncertainty such as the cube mass and freestream dynamic pressure are also present, however these are likely small relative to the optical tracking uncertainties. Nevertheless, our CFD data, correlations, and the experimental data from [5] are all in good agreement, and the comparison to experimental results from [5] provides further confidence in the accuracy of our correlations.

V. Conclusion

In this work, we develop correlations for aerodynamic force and moment coefficients of a cube in Mach 6 flow, valid for all possible incident flow angles. Force and moment coefficients are calculated numerically using the CFD solver, Eilmer. Sixteen independent cube orientations are simulated using the Fawkes computing cluster. The data is then extended to cover all possible incident flow angles by exploiting the symmetry of the cube geometry.

Correlations for the data are developed using sparse regression with the LASSO algorithm. Basis functions using spherical harmonics form the regressors, ensuring the aerodynamic coefficients are modelled as a function of the polar incident flow angles efficiently. Spherical harmonics were found to effectively capture the shape of the aerodynamic surfaces with relatively few terms compared to alternatives (between 8 and 25 regression coefficients). The regression introduces a maximum 3σ regression error 12% of the maximum C_{Mi} , improving on past studies.

The accuracy of the correlations is validated through comparison to Mach 6 free-flight experiments conducted in the TUSQ wind tunnel. Over the wide range of incident flow angles in the experimental data, the maximum error was $\Delta||C_F|| = 0.12$, and $\Delta||C_M|| = 0.032$. The correlations were then validated further through comparison to a second experimental data-set from Mach 7 free-flight experiments in the H2K wind tunnel. The correlations were found to be accurate for Mach 7 flow over a 90° angle of attack sweep, with a maximum error of $\Delta C_{F_x^L}, \Delta C_{F_z^L} = 0.01$ and $\Delta C_{M_y^L} = 0.008$. Comparison to additional CFD results suggests small improvements in the correlations can still be realised. Overall, the correlations were found to be accurate against multiple experimental data-sets, enabling trajectory calculations for cubes with 6 degrees-of-freedom in hypersonic flow. These trajectory calculations are valuable for orbital debris re-entry problems where high fidelity predictions may improve debris field estimates.

Future work should involve the application of this approach to more space debris representative geometries with symmetry. Additional work to investigate the sensitivity of the computational approach against cube edge rounding (even and uneven) and the assumption of laminar, quasi-steady inflow can be conducted. Finally, the developed correlations should be expanded to a larger flight envelope (Mach number, Reynolds number) in the future.

Acknowledgments

This research was supported under the Australian Research Council's Discovery Project funding scheme (Project DP220102751 - Dispersion of Spacecraft Components During Re-entry). Aspects of this work were also supported by the Australian Government Research Training Program. Numerical simulations were undertaken using the University of Southern Queensland (UniSQ) Fawkes HPC which is co-sponsored by QCIF (Queensland Cyber Infrastructure Foundation) – www.usq.edu.au/hpc. The authors would also like to extend their thanks to Reader Peter Jacobs for his support with Eilmer.

References

- [1] Yamaguchi, T., Yoshikawa, M., Yagi, M., and Tholen, D. J., "Entry Dispersion Analysis for the HAYABUSA Spacecraft using Ground-Based Optical Observation*," *Publications of the Astronomical Society of Japan*, Vol. 63, No. 5, 2011, pp. 979–985. <https://doi.org/10.1093/pasj/63.5.979>.
- [2] Reyhanoglu, M., and Alvarado, J., "Estimation of debris dispersion due to a space vehicle breakup during reentry," *Acta Astronautica*, Vol. 86, 2013, pp. 211–218. <https://doi.org/10.1016/j.actaastro.2013.01.018>.
- [3] Wu, Z., Hu, R., Qu, X., Wand, X., and Wu, Z., "Space Debris Reentry Analysis Methods and Tools," *Chinese Journal of Aeronautics*, Vol. 24, No. 4, 2011, pp. 387–395. [https://doi.org/10.1016/S1000-9361\(11\)60046-0](https://doi.org/10.1016/S1000-9361(11)60046-0).
- [4] Rafano Carná, S., and Bevilacqua, R., "High fidelity model for the atmospheric re-entry of CubeSats equipped with the Drag De-Orbit Device," *Acta Astronautica*, Vol. 156, 2019, pp. 134–156. <https://doi.org/10.1016/j.actaastro.2018.05.049>.
- [5] Seltner, P. M., Willems, S., and Gülhan, A., "Aerodynamic Coefficients of Free-Flying Cubes in Hypersonic Flowfield," *Journal of Spacecraft and Rockets*, Vol. 56, No. 6, 2019, pp. 1725–1734. <https://doi.org/10.2514/1.A34345>.
- [6] Seltner, P. M., Willems, S., Gülhan, A., Stern, E. C., Brock, J. M., and Aftosmis, M. J., "Aerodynamics of inclined cylindrical bodies free-flying in a hypersonic flowfield," *Experiments in Fluids*, Vol. 62, 2021. <https://doi.org/10.1007/s00348-021-03269-6>.
- [7] Grauer, J. A., and Morelli, E. A., "A Generic Nonlinear Aerodynamic Model for Aircraft," *AIAA Atmospheric Flight Mechanics Conference*, AIAA, 2014. <https://doi.org/10.2514/6.2014-0542>.
- [8] Dowell, E. H., "Eigenmode analysis in unsteady aerodynamics - Reduced-order models," *AIAA Journal*, Vol. 34, No. 8, 1996, pp. 1578–1583. <https://doi.org/10.2514/3.13274>.
- [9] Lorente, L. S., Vega, J. M., and Velazquez, A., "Generation of Aerodynamics Databases Using High-Order Singular Value Decomposition," *Journal of Aircraft*, Vol. 45, No. 5, 2008, pp. 1779–1788. <https://doi.org/10.2514/1.35258>.
- [10] "Compression of aerodynamic databases using high-order singular value decomposition," *Aerospace Science and Technology*, Vol. 14, No. 3, 2010, pp. 168–177. <https://doi.org/10.1016/j.ast.2009.12.003>.

- [11] Leng, G., “Compression of aircraft aerodynamic database using multivariable Chebyshev polynomials,” *Advances in Engineering Software*, Vol. 28, No. 2, 1997, pp. 133–141. [https://doi.org/10.1016/S0965-9978\(96\)00043-9](https://doi.org/10.1016/S0965-9978(96)00043-9).
- [12] de Visser, C., Mulder, J., and Chu, Q., “Global Nonlinear Aerodynamic Model Identification with Multivariate Splines,” *AIAA Atmospheric Flight Mechanics Conference*, AIAA, 2009. <https://doi.org/10.2514/6.2009-5726>.
- [13] Ritchie, D. W., and Kemp, G. J. L., “Fast computation, rotation, and comparison of low resolution spherical harmonic molecular surfaces,” *Journal of Computational Chemistry*, Vol. 20, No. 4, 1999, p. 383 – 395. [https://doi.org/10.1002/\(SICI\)1096-987X\(199903\)20:4<383::AID-JCC1>3.0.CO;2-M](https://doi.org/10.1002/(SICI)1096-987X(199903)20:4<383::AID-JCC1>3.0.CO;2-M).
- [14] Boomsma, W., and Frellsen, J., “Spherical convolutions and their application in molecular modelling,” *Advances in Neural Information Processing Systems*, Vol. 30, edited by I. Guyon, U. V. Luxburg, S. Bengio, H. Wallach, R. Fergus, S. Vishwanathan, and R. Garnett, Curran Associates, Inc., 2017.
- [15] Nortje, C. R., Ward, W. O. C., Neuman, B. P., and Bai, L., “Spherical Harmonics for Surface Parametrisation and Remeshing,” *Mathematical Problems in Engineering*, Vol. 2015, 2015. <https://doi.org/10.1155/2015/582870>.
- [16] Lock, A., Armstrong, G., Hack, F., Birch, B., Buttsworth, D., and Jahn, I. H., “Optical aerodynamic measurements of hypersonic free-flight using Bayesian state estimation,” *AIAA AVIATION 2023 Forum*, American Institute of Aeronautics and Astronautics, 2023. <https://doi.org/10.2514/6.2023-3713>.
- [17] Lock, A., Hack, F., Jahn, I., Armstrong, G., Birch, B., and Buttsworth, D., “Aerodynamic Measurements of Hypersonic Free-Flight via Optical Tracking and Bayesian State Estimation,” *AIAA Journal*, Vol. 0, No. 0, 0, pp. 1–16. <https://doi.org/10.2514/1.J064061>.
- [18] Gibbons, N. N., Damm, K. A., Jacobs, P. A., and Gollan, R. J., “Eilmer: An open-source multi-physics hypersonic flow solver,” *Computer Physics Communications*, Vol. 282, 2023, p. 108551. <https://doi.org/https://doi.org/10.1016/j.cpc.2022.108551>, URL <https://www.sciencedirect.com/science/article/pii/S0010465522002703>.
- [19] Butler, C. S., Whalen, T. J., Sousa, C. E., and Laurence, S. J., “Dynamics of a spherical body shedding from a hypersonic ramp. Part 2. Viscous flow,” *Journal of Fluid Mechanics*, Vol. 906, 2021, p. A29. <https://doi.org/10.1017/jfm.2020.757>.
- [20] Marwege, A., Willems, S., Gülhan, A., Aftosmis, M. J., and Stern, E. C., “Superposition Method for Force Estimations on Bodies in Supersonic and Hypersonic Flows,” *Journal of Spacecraft and Rockets*, Vol. 55, No. 5, 2018, pp. 1166–1180. <https://doi.org/10.2514/1.A34128>.
- [21] Wada, Y., and Liou, M., “A Flux Splitting Scheme with High-Resolution and Robustness for Discontinuities,” *32nd Aerospace Sciences Meeting and Exhibit*, American Institute of Aeronautics and Astronautics, 1994. <https://doi.org/10.2514/6.1994-83>.
- [22] Haenel, D., Schwane, R., and Seider, G., “On the accuracy of upwind schemes for the solution of the Navier-Stokes equations,” *8th Computational Fluid Dynamics Conference*, American Institute of Aeronautics and Astronautics, 1987. <https://doi.org/10.2514/6.1987-1105>.

- [23] De Pontieu, B., “Database of photometric periods of artificial satellites,” *Advances in Space Research*, Vol. 19, No. 2, 1997, pp. 229–232. [https://doi.org/10.1016/S0273-1177\(97\)00005-7](https://doi.org/10.1016/S0273-1177(97)00005-7), space Debris.
- [24] Kita, N., Cliquet, G., and Miyata, K., “Mapping two-dimensional plots to a spherical surface using elliptical grid mapping,” *Graphical Models*, Vol. 109, 2020, p. 101067. <https://doi.org/10.1016/j.gmod.2020.101067>.
- [25] Buttsworth, D., “Ludwig Tunnel Facility with Free Piston Compression Heating for Supersonic and Hypersonic Testing,” *9th Australian Space Science Conference*, National Space Society of Australia Ltd, 2010, pp. 153–162.
- [26] Birch, B., Buttsworth, D., Choudhury, R., and Stern, N., “Characterization of a Ludwig Tube with Free Piston Compression Heating in Mach 6 Configuration,” *22nd AIAA International Space Planes and Hypersonics Systems and Technologies Conference*, American Institute of Aeronautics and Astronautics, 2018. <https://doi.org/10.2514/6.2018-5266>.
- [27] Birch, B., Buttsworth, D., and Zander, F., “Measurements of Freestream Density Fluctuations in a Hypersonic Wind Tunnel,” *Experiments in Fluids*, Vol. 61, No. 158, 2020. <https://doi.org/10.1007/s00348-020-02992-w>.
- [28] Birch, B., Buttsworth, D., and Zander, F., “Time-Resolved Stagnation Temperature Measurements in Hypersonic Flows Using Surface Junction Thermocouples,” *Experimental Thermal and Fluid Science*, 2020, p. 110177. <https://doi.org/10.1016/j.expthermflusci.2020.110177>.
- [29] International Civil Aviation Organisation, *Manual of the ICAO Standard Atmosphere - extended to 80 kilometres / 262,500 feet (Doc 7488)*, 1993.
- [30] Roache, P., *Verification and Validation in Computational Science and Engineering*, Hermosa Publishers, Socorro, NM, 1998.
- [31] Stern, F., Wilson, R., Coleman, H., and Paterson, E., “Comprehensive Approach to Verification and Validation of CFD Simulations-Part 1: Methodology and Procedures,” *Journal of Fluids Engineering*, Vol. 123, 2001. <https://doi.org/10.1115/1.1412235>.
- [32] Abramowitz, M., and Stegun, I., *Handbook of Mathematical Functions: With Formulas, Graphs, and Mathematical Tables*, Applied mathematics series, Dover Publications, 1965. <https://doi.org/10.5555/1098650>.
- [33] Tibshirani, R., “Regression Shrinkage and Selection Via the Lasso,” *Journal of the Royal Statistical Society: Series B (Methodological)*, Vol. 58, No. 1, 1996, pp. 267–288. <https://doi.org/10.1111/j.2517-6161.1996.tb02080.x>.
- [34] Lock, A., “Dry cooling for supercritical carbon dioxide power cycles,” Ph.D. thesis, The University of Queensland, 2023. <https://doi.org/10.14264/9e992e9>.
- [35] Hoerner, S., *Fluid-dynamic Drag: Practical Information on Aerodynamic Drag and Hydrodynamic Resistance*, Hoerner Fluid Dynamics, Bakersfield, CA, 1965, pp. 16.14–16.16.